

Machine Learning S-wave Scattering Phase Shifts Bypassing the Radial Schrödinger Equation

Alessandro Romualdi*

Gionni Marchetti†

Departament de Física de la Matèria Condensada,

Universitat de Barcelona,

Carrer Martí i Franquès 1, 08028, Barcelona, Spain

and

National Institute of Chemical Physics and Biophysics,
Rävala 10, 10143, Tallinn, Estonia

(Dated: June 7, 2022)

We present a *proof of concept* machine learning model resting on a convolutional neural network capable to yield accurate scattering s-wave phase shifts caused by different three-dimensional spherically symmetric potentials at fixed collision energy thereby bypassing the radial Schrödinger equation. In our work, we discuss how the Hamiltonian can serve as a guiding principle in the construction of a physically-motivated descriptor. The good performance, even in presence of bound states in the data sets, exhibited by our model that accordingly is trained on the Hamiltonian through each scattering potential, demonstrates the feasibility of this proof of principle.

Phase shifts play a key role in the partial wave analysis, and are the crucial quantities for obtaining the scattering amplitude by which the elastic scattering properties of the physical or chemical system of interest can be calculated^{1,2}. In particular, phase shifts δ_0 in s-wave, i.e., when the angular momentum number $l = 0$, are significant for atomic collisions in ultracold regime where the s-wave scattering channel dominates^{3–5}. Moreover, in Coulomb systems the s-wave phase shift allows the δ_l with $l = 1, 2, \dots$ to be recursively determined starting from the knowledge of δ_0 ⁶.

Therefore their accurate computation is in great demand in the various fields of science. In this regard it is worth noting that Kohn developed one of the most used method for accurately computing the phase shifts based on the variational principle and the Schrödinger equation^{1,7,8}, and very recently a new method and new computer code, based on a recurrence relation and the variable phase method (VPM)^{9–12}, respectively, aiming at the same task have been put forward^{6,13}.

While the traditional numerical methods such as the one presented in Ref.¹³ are based on the algorithms which numerically integrate the Schrödinger equation for a given scattering potential V^{sc} , we herein propose a supervised machine learning (ML) approach for yielding accurate phase shifts through the empirical fitting of data, therefore bypassing the radial Schrödinger equation (SE). Although our work is, to some extent, motivated by the recent advances of ML and its applications to physics, chemistry and materials science^{14–16} which prove successful in yielding accurate predictions of physical quantities, such as the molecular ground state energy^{17,18}, polarizability¹⁹, atomization energy²⁰, density of states at Fermi energy of crystalline solids²¹, identification of the phases of matter^{22–24}, development of ML potentials^{25–29} and

construction of deep-learning wavefunctions of the electronic Schrödinger equation^{30,31}, its purpose is essentially different being a *proof of concept* (see Fig. 1). Indeed, in this paper we wish to address the crucial role played by the Hamiltonian H for constructing a physically motivated descriptor (or fingerprint)^{32–35}. First, the Hamiltonian contains all the possible physical information about the system under scrutiny³⁶ e.g., the symmetries such as the translations and rotations under which it is invariant. Second, the physical scale over which the phenomena occur is naturally provided to the descriptor without the need to heuristically determine *ad hoc* cut-offs as routinely done for the atomistic systems^{29,35}.

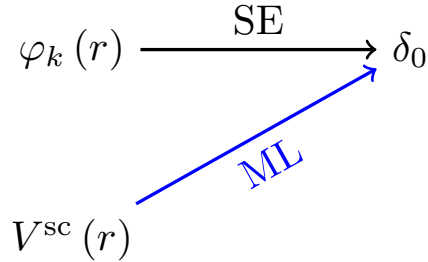


FIG. 1. A Schematic view of our *proof of concept*. Our ML model is trained on the Hamiltonian, through the scattering potential $V^{\text{sc}}(r)$ and not on the phase function $\varphi_k(r)$ in the real space, for learning the scattering phase shifts δ_0 at a given wave number k . Instead, the standard approach is to numerically integrate the radial Schrödinger equation for yielding $\varphi_k(r)$ and the corresponding asymptotic δ_0 with initial condition $\delta_0(0) = 0$ at the origin, i.e. at $r = 0$.

To support the above observations, first we shall limit ourselves to the regression task that involve the prediction of the quantum phase shifts δ_0 at a fixed collision energy in the presence of a three-dimensional spherically symmetric regular potential. In such a case the Hamiltonian reads $H = T + V^{\text{sc}}$, where T and V^{sc} are the kinetic energy and the scattering potential, respectively. Therefore the scattering potential V^{sc} uniquely determines the Hamiltonian H^{37} . This situation is analogous to that thereby the Coulomb Matrix (CM) descriptor^{20,38} is built on. Indeed, the CM's entries correspond to the Coulomb terms of the external potential in the molecular Hamiltonian.

Second, our ML model consists in a convolutional neural network (CNN) trained on the Hamiltonian, through the scattering potential V^{sc} and not on the phase function φ_k that can be obtained only by solving the radial Schrödinger equation (see Fig. 1). Accordingly, the regression task for the phase shifts will be performed by feeding images X of V^{sc} instances together with their labels δ_0 to the CNN. It is worth noting that our machine model is somehow equivalent to that employed by Mills et al.³⁹ to predict ground-state energy of an electron in confining two-dimensional electrostatic potentials.

Overall, our machine learning model is capable of predicting the target phase shifts, caused by different three-dimensional spherically symmetric regular potentials at fixed collision energy with relative error much less than 1%, and corresponding ML accuracy in terms of the average of the mean absolute percentage error (MAPE) $\lesssim 0.1\%$. This is remarkable, considering that the approximate phase shifts computed in the first Born approximation and the exact ones are considered to agree very well when the relative error is $\lesssim 5\%$ ¹.

Although our findings are a consequence of the universal approximation theorem for the neural networks⁴⁰ which suggests that the continuous mapping between the scattering potential $V^{\text{sc}}(r)$ in the real space and the corresponding phase shift $\delta_0(r)$ can be learned by means of a feed-forward CNN^{41,42}, similar to that successfully used in image recognition tasks^{43–48}, they do support the idea that the Hamiltonian of any given system should serve as a guiding principle in the search for physically-motivated descriptors for ML applications to physical sciences.

Note that throughout this paper the computations were performed assuming the typical scattering units, that is, $\hbar = 2m = 1$, m being the reduced mass of the scattering particle. Therefore in such units k , k^2 are the wave number and energy of the scattering particle in the center of mass reference frame, respectively.

I. METHODS

A. Three-Dimensional Spherically Symmetric Potentials

In order to address the problem of learning quantum scattering phase shifts from data, we consider three-dimensional spherically symmetric potentials that satisfy some nice mathematical properties in accordance with the scattering theory. In particular, the latter requires the scattering potentials to be reasonable smooth functions of the interparticle distance and to fall off sufficiently fast in the asymptotic region¹⁰.

In the present work our choice of the potentials was dictated by their theoretical and practical importance in various branches of physics and chemical physics. In the following we briefly list the potentials under scrutiny.

The Thomas-Fermi (TF) potential (or Yukawa potential) V^{TF} accounts for the screened Coulomb interaction and the strong interaction in condensed matter systems^{49–51} and nuclear and particle physics⁵², respectively. In its attractive form this potential has the following expression $V^{\text{TF}}(r) = -V_0^{\text{TF}} \exp(-qr)/r$ where the positive quantities r, q, V_0^{TF} denote the interparticle distance, the screening parameter and the potential's strength, respectively.

A linear combination of the TF potentials gives rise to a scattering potential of significant importance in nuclear and condensed matter physics^{53,54}. Here we shall consider a double Yukawa (DY) potential V^{DY} which is just a linear combination of two TF potentials, i.e. $V^{\text{DY}}(r) = -V_{01} \exp(-q_1 r)/r + V_{02} \exp(-q_2 r)/r$. In this paper we shall tune the parameters q, V_{01}, V_{02} in such a way that it will be repulsive and attractive at short and long distances, respectively¹⁰, see Section 1C for details.

In plasma physics the screened Coulomb interaction is often accounted for by means of the exponential cosine (EC) screened Coulomb potential $V^{\text{EC}}(r) = V_0^{\text{EC}} \exp(-qr) \cos(qr)/r^{55–61}$. Note that both potentials V^{EC} and V^{TF} derive directly from the random phase approximation (RPA), thus neglecting the short-range exchange and correlation effects in electronic systems⁵¹.

Finally, our study will include the square-well (SW) potential V^{SW} that plays a fundamental role in the modeling of short-range interactions in various physical systems. In particular, the SW potential is useful as first approximation to the nuclear interaction between a neutron and a proton in a deuteron⁶². The attractive V^{SW} is defined by⁶³

$$V^{\text{SW}} = \begin{cases} -V_0, & r \leq a \\ 0, & r > a \end{cases} \quad (1)$$

where the positive quantities V_0, a defines the SW potential's depth and radius, respectively. For a given collision energy k^2 , the phase shift δ_0 is given by⁶³

$$\tan \delta_0 = \frac{k j'_0(ka) j_0(\alpha a) - \alpha j_0(ka) j'_0(\alpha a)}{k n'_0(ka) j_0(\alpha a) - \alpha n_0(ka) j'_0(\alpha a)}, \quad (2)$$

where the prime denotes differentiation with respect to the function's argument, and $\alpha^2 = k^2 + V_0$. Here the symbols j_0, n_0 denote the spherical Bessel functions. Note that Eq. 2 is beset by modulo π ambiguity, i.e. δ_0 is defined up to addition of an arbitrary multiple of $\pi^{64,65}$.

B. Computation of the Quantum Phase Shifts: The Variable Phase Approach

The standard computation of the phase shifts takes place in two stages. First, given a spherically symmetric regular potential $V^{\text{sc}}(r)$, one needs to solve the radial Schrödinger equation

$$u_l''(r) + [k^2 - V^{\text{cf}}(r) - V^{\text{sc}}(r)] u_l(r) = 0, \quad (3)$$

for $u_l(r)$ with the initial condition $u_l(0) = 0$ at the origin for a given angular momentum number l ($l = 0, 1, \dots$). The repulsive centrifugal potential $V^{\text{cf}}(r) = l(l+1)/r^2$ vanishes in our case as we shall limit ourselves to the computation of the s-wave phase shift δ_0 only. Therefore Eq. 3 in s-wave becomes

$$u_0''(r) + [k^2 - V^{\text{sc}}(r)] u_0(r) = 0. \quad (4)$$

The solution u_0 can be obtained by numerically integrating Eq. 4. Note that this task requires the knowledge of the range of V^{sc} in order to avoid possible inaccuracies and round-off errors as well. Finally, the quantity δ_0 is obtained by matching the numerical solution with the free solution of Eq. 4 in the asymptotic region, i.e., where the effects of V^{sc} are negligible. As a consequence one needs to solve an algebraic equation for δ_0 of the same kind of Eq. 2, thereby involving the spherical Bessel functions j_0, n_0 , and their corresponding derivatives. In general, the above standard approach can be cumbersome to be implemented for in-house computer codes.

An alternative approach to the computation of the phase shifts is given by the variable phase method^{9–11,66}. Despite the fact that the VPM follows from a simple mathematical property, that is, a homogeneous second order differential equation such as the radial Schrödinger equation can be reduced to a first order nonlinear equation of Riccati type, it really presents a paradigmatic shift in the partial wave analysis as the phase shifts are no longer regarded as mere scalar quantities. In fact, not only the VPM yields the value of the phase shift directly, but promotes it from a scalar quantity to a phase function $r \mapsto \delta_0(r)$, so providing important physical insights about the collision effects due to the presence of a particular potential¹⁰.

The variable phase method rests on the following differential equation for the function $\delta_0(r)$

$$\delta_0'(r) = -\frac{V^{\text{sc}}(r)}{k} \left[\cos \delta_0(r) \hat{j}_0(kr) - \sin \delta_0(r) \hat{n}_0(kr) \right]^2, \quad (5)$$

with the boundary condition at the origin $\delta_0(0) = 0$. In Eq. 5 the symbols \hat{j}_0, \hat{n}_0 denote the Riccati-Bessel functions.

The numerical integration of Eq. 5 yields the value of δ_0 directly by taking the asymptotic limit of the solution, i.e. $\lim_{r \rightarrow \infty} \delta_0(r) = \delta_0^{10,67}$. Moreover, the VPM automatically removes the modulo π ambiguity^{10,67,68}. The latter property gives the following expression for the Levinson's theorem^{10,69}

$$\lim_{k \rightarrow 0} \delta_0(k) = n_{b,0}\pi, \quad (6)$$

where $n_{b,0}$ is the number of bound states that the scattering potential is capable to form in s-wave at low energy.

In Fig. 2 the phase shift δ_0 as function of r due to the presence of an attractive TF potential with $V_0^{\text{TF}} = 5$, $q = 1.1$ obtained by means of the VPM for $k = 0.1$ is shown. It is evident that after an abrupt change the phase function $\delta_0(r)$ converges to $\delta_0 \approx \pi$ in the asymptotic region. Therefore, according to Levinson's theorem, see Eq. 6, this TF potential's instance supports one bound state in s-wave. In such a case its respective phase function takes a typical step-like behaviour^{10,70} as displayed in Fig. 2. However, the information about the presence of one or more bound states can be completely lost by looking only at the shape of the phase function, when the collision energy is increased. This fact is illustrated in Fig. 2 by means of the plot of the phase function's curve corresponding to the above TF potential's instance obtained at $k = 10$.

Also, in Fig. 2 the phase function's curves corresponding to the EC and DY potentials with $V_0^{\text{EC}} = 5, q = 1.8$ and $V_{02} = 2V_{01} = 20, q_2 = 2q_1 = 2.0$, computed at $k = 0.1$ and $k = 0.5$, respectively, are displayed. All the curves in Fig. 2, see also Table I for details, correspond to scattering potentials' instances chosen at random from the respective data sets on which the CNN are trained. They clearly exemplify the different learning tasks that the CNN has to undertake in order to approximate $r \mapsto \delta_0(r)$ at given collision energy k^2 for the scattering potential V^{sc} under scrutiny.

C. Image of the Scattering Potential Instance as Suitable Descriptor

In our ML model, the descriptor of a scattering potential V^{sc} 's instance is an image X of N pixels, i.e., its dimension N is the resolution of such an image, containing the values of this potential evaluated at N different points within a discretized support interval $I_s = [r_0, r_1, r_2, \dots, r_N]$, i.e., $X =$

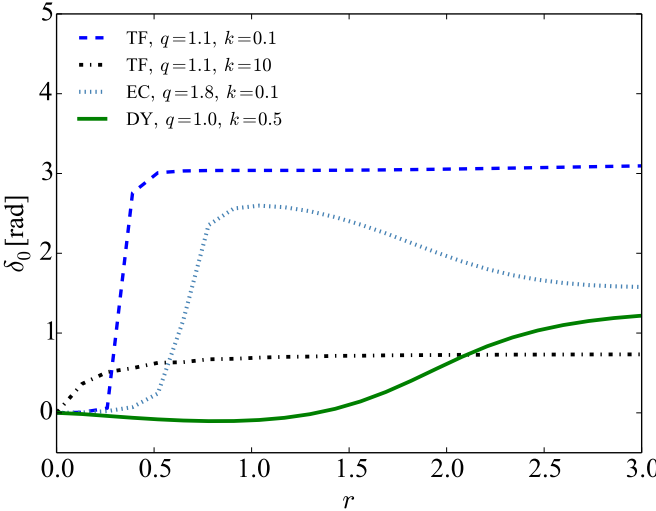


FIG. 2. The phase shift δ_0 as function of r caused by the TF, EC, DY potentials' instances chosen at random from the data sets, computed by means of the VPM for different values of k and q of interest. We refer the reader to Table I for all the information about the potentials' parameters, and their respective asymptotic values of δ_0 .

TABLE I. The strengths and screening parameters of the TF, EC, DY potentials along with the respective asymptotic phase shifts computed by means of the VPM at different values of k are shown, respectively. Note that $V_{02} = 2V_{01} = 20$ and $q_2 = 2q_1 = 2.0$ for the DY potential.

V^{sc}	parameters	k	δ_0
V^{TF}	$V_0^{TF} = 5, q = 1.1$	0.1	3.15
V^{TF}	$V_0^{TF} = 5, q = 1.1$	10	0.73
V^{EC}	$V_0^{EC} = 5, q = 1.8$	0.1	1.61
V^{DY}	$V_{01} = 10, q_1 = 1.0$	0.5	1.28

$[V^{sc}(r_0), V^{sc}(r_1), V^{sc}(r_2), \dots, V^{sc}(r_N)]$. The minimum r_0 and the maximum r_N of the set I_s are chosen according to the typical behaviour of the scattering potential V^{sc} in the neighborhood of the origin and its asymptotic regime, respectively. Thus, for a fixed strength of V^{sc} the resolution N would determine a coarse-grained view of such a potential, thereby causing the image's details to vary smoothly with the screening parameter q . In Fig. 3 six images X corresponding to different instances of V^{DY} with parameters $V_{01} = 10, V_{02} = 20$ and $q_1 \equiv q, q_2 = 2q$ ($q \in [1, 2]$) such that it is repulsive at short distance and attractive in the asymptotic region, are shown. Our proposed descriptor offers a good compromise between the accuracy and the computation time.

However, it is not possible to apply such a representa-

tion to the potential V^{SW} as its image on the discretized interval I_s would not always encode small variations with respect to its screening parameter $1/a$. To overcome this issue we shall resort to the effective range approximation^{62,71} that holds for very small values of k only, see Section II for details.

Finally, it is worth noting that the statistical learning performed by the CNN will be done assuming that each scattering potential's strength is fixed. The reason is that the phase shift δ_0 caused by an instance of the same potential but with a different strength can be directly derived by an appropriate scaling¹⁰.

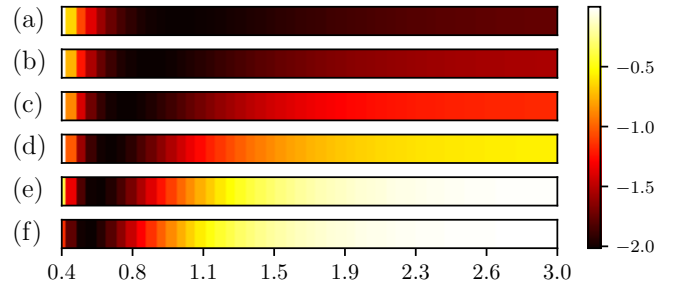


FIG. 3. The images X labelled by (a), (b), (c), (d), (e), (f) relative to the scattering potential V^{DY} with $V_{01} = 10, V_{02} = 20$ and $q_1 \equiv q, q_2 = 2q$ obtained for $q = 1.0, 1.2, 1.42, 1.62, 1.8, 1.99$, respectively. The color (pixel intensity) indicates the value of the potential.

D. Data Sets

For each scattering potential, except the SW potential, a data set $D_k = \{(X_1, \delta_0^{(1)}), (X_2, \delta_0^{(2)}), \dots, (X_n, \delta_0^{(n)})\}$ where $n = 1000$ is constructed for $k = 0.1, 0.5, 5, 10$, respectively. Each image descriptor X_μ is labelled by the corresponding phase shift $\delta_0^{(\mu)}$ computed at fixed wave number k by means of the VPM whose implementation rests on the algorithm LSODA^{13,72}. We divide each data set D_k into training, validation and test sets. The CNN's learning is performed within the training set, while the validation set is used to adjust the model hyperparameters by studying the model convergence during the learning phase. Finally, the assessment of the CNN's accuracy is performed on the test set.

The TF and EC potentials' parameters upon which the respective data set D_k are constructed are $V_0^{TF} = V_0^{EC} = 5$ and q being uniformly generated in $[0.5, 2.5]$ and $[0.5, 2]$, respectively. According to this choice of parameters some instances of TF potential can form s-wave bound states, while each instance of EC potential cannot support them. In this regard, we estimated that roughly 30% instances of TF potentials in $D_{0.1}$ can form one bound state.

The parameters of interest for the DY potential were introduced in Section IC. In the latter case the screening parameter q_1 is uniformly chosen at random in $[1, 2]$.

Note that none of the DY potential's instances is capable of forming bound states.

Finally, two data sets of shallow SW potentials with depth $V_0 = 0.25$ and radii a uniformly chosen in $[0.4, 2]$ are generated computing the respective s-wave phase shifts according to Eq. 2 at $k = 0.01, 0.1$.

E. Convolutional Neural Network

Our model is composed of a linear stack of $L = 5$ one-dimensional convolutional layers each followed by a max-pooling layer. In each convolutional layer different numbers of filters, each of size 3 pixels, take the output of the previous layer (or the input image in case of the first layer) and extract features while scanning one pixel at time. Each convolution is followed by the Rectified Linear Unit (ReLU) activation. In this way, the computation units of a convolutional layer create feature maps that summarise the presence of relevant details in the input images.

After each convolution layer, a max-pooling layer encapsulates the most activated output of the feature map, resulting in a down sampled representation of the layer input. As the information is processed through the layers of the network, convolutional and max-pooling operations make the model able to capture patterns of progressively higher complexity. Hence the number of filters in each layer are progressively increased to allow more abstraction. In particular, we used 64, 128, 256, 256, 256 filters on the first to the last convolutional layer, respectively. At the end of the network a series or two fully connected layers, the first one with output size 1024, and the last one with a single output, perform label prediction based on the features extracted by the last max-pooling layer. The CNN have been implemented on TensorFlow⁷³ (version 2.4.0), and trained by means of the Adam optimizer⁷⁴.

II. RESULTS AND DISCUSSION

In order to assess the CNN's performance over the above data sets we adopt two estimator measures: the mean square error (MSE) and mean absolute percentage error. First, we train the CNN by minimizing the MSE during the training phase using the Adam optimizer. Second, we report the MAPE between the true and predicted phase shifts in the test set as a measure of model performance. Note that unless differently specified, the training happened over 100 epochs on 16 mini batch using a learning rate of 1×10^{-4} .

In panels (a), (b), (c), (d) of Fig. 4, Fig. 5 and Fig. 6 the scatter plots of the prediction versus the reference s-wave phase shift caused by TF, DY, and EC, respectively, at $k = 0.1, 0.5, 5, 10$ are shown. For all these potentials the MAPE is comparable and varies from 0.01% to 0.03% when the learning occurs for $k = 0.5, 5, 10$. There is

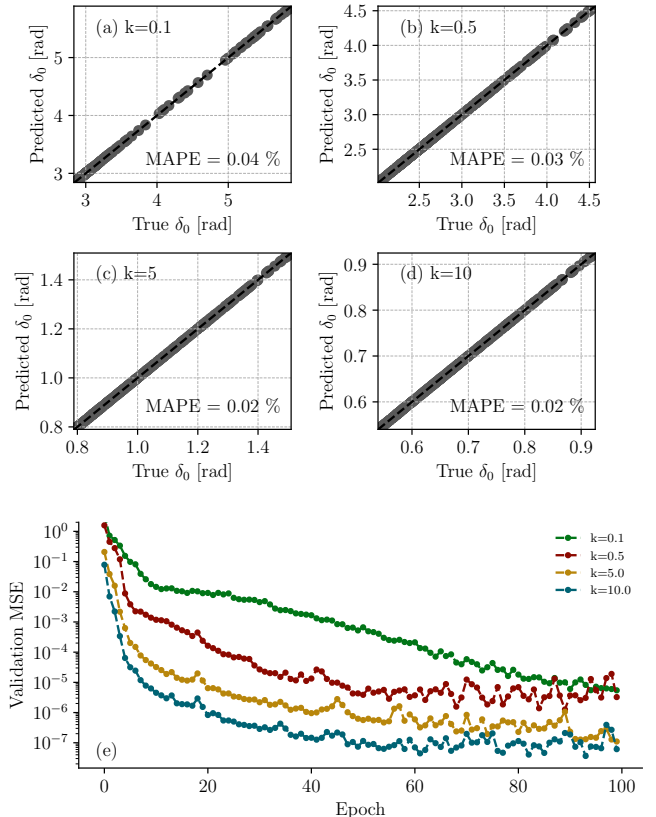


FIG. 4. In panels (a), (b), (c), (d) predictions versus reference phase shifts δ_0 caused by the TF potential at $k = 0.1, 0.5, 5, 10$, respectively, are shown. Panel (e) displays the relative learning curves as functions of the training epochs.

a plausible physical explanation of these similar learning performance obtained despite the different functional form of the scattering potentials under study. The reason is that increasing the energy for the screening parameters under scrutiny each scattering potential affects the phase function in the neighbourhood of the origin only. To understand this, one just needs to look at the scatter plot relative to DY potential in panels (c) and (d) of Fig. 5 where the phase shifts are negative. This happens because the repulsive part of the DY potentials' instances mainly affect the phase function nearby the origin as a consequence to our choice of the screening parameters. On the other hand, by inspections of some instances of the TF, DY, and EC potentials' data sets we found that for the parameters of interest, increasing the energy the phase function $r \mapsto \delta_0(r)$ takes a smooth form for each V^{sc} . For instance, this smooth behaviour is illustrated by the plot of the phase function due to a TF potential's instance at $k = 10$ in Fig. 2. Thus, the CNN's learning task become easier at higher collision energies, that is, increasing k . On the other hand this observation is confirmed looking at the learning curves as functions of

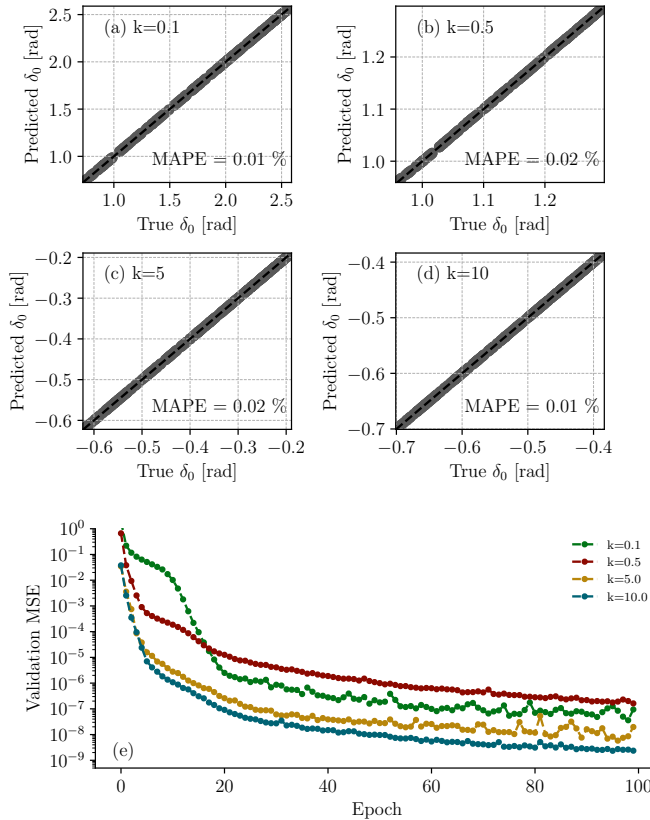


FIG. 5. In panels (a), (b), (c), (d) predictions versus reference phase shifts δ_0 caused by the DY potential at $k = 0.1, 0.5, 5, 10$, respectively, are shown. Panel (e) displays the relative learning curves as functions of the training epochs.

epochs shown in panel (e) of Fig. 4, Fig. 5 and Fig. 6 for $k = 5, 10$ where a far smaller number of training epochs with respect to that observed for $k = 0.1, 0.5$ is necessary for achieving the convergence. As a consequence the MAPE increases at low energies.

As the Adam optimizer algorithm takes considerably more epochs to converge over the data set corresponding to small values of k , it is evident that the CNN's learning task becomes difficult. This can be easily understood looking at the data set $D_{0.1}$ for the Thomas-Fermi potential V^{TF} . In such a case we know that it contains about 30% of V^{TF} instances supporting one bound state. Therefore in such a case the CNN need to approximate a phase function $\delta_0(t)$ presenting an abrupt change due to the emergence of a plateau where $\delta_0 \approx \pi$ for certain values of the screening parameter q . We illustrated this characteristic behaviour due to presence of the bound states in Section 1B (see also Fig. 2). Moreover, the phase functions relative to V^{EC} and V^{DY} certainly exhibit a far richer functional form at low energy as illustrated by two respective phase functions chosen at random in Fig. 2. In particular, some V^{EC} instances can be

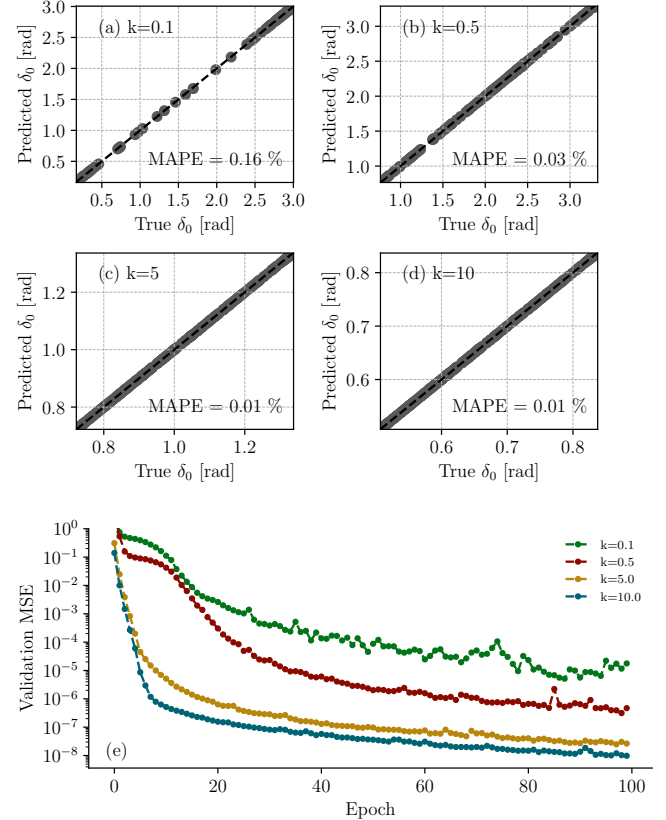


FIG. 6. In panels (a), (b), (c), (d) predictions versus reference phase shifts δ_0 caused by the EC potential at $k = 0.1, 0.5, 5, 10$, respectively, are shown. Panel (e) displays the relative learning curves as functions of the training epochs.

repulsive, attractive and repulsive, respectively, in three different contiguous regions, respectively. This behaviour increases the functional complexity of the phase function, thus explaining the reason for which the largest MAPE ≈ 0.16 is obtained for the EC potential at $k = 0.1$ (see the relative scatter plot in panel (a) of Fig. 6).

Overall, the previous observations explain why the CNN's performance in general worsens slightly at small values of k . Despite this fact, our ML model yields accurate predictions of the phase shifts caused by TF, EC, DY potentials with relative error that is much less than 1%.

As explained in Section 1C it is not possible to meaningfully represent the SW potential as an image in our approach. To overcome this issue, we can resort the effective range approximation for short-range potentials^{62,71} that is applicable in s-wave scattering at low energy, i.e., $k \approx 0$. This approximation reads as⁷¹

$$k \cot \delta_0 \approx -\frac{1}{c_0} + \frac{1}{2} k^2 r_0, \quad (7)$$

where c_0, r_0 are called the scattering length and the ef-

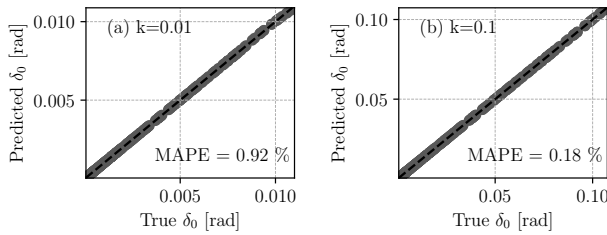


FIG. 7. In panels (a), (b) predictions versus reference phase shifts δ_0 caused by the SW potential replaced by the TF potential according to the shape independent approximation at $k = 0.01, 0.1$, respectively, are shown.

fective range, respectively. In general, for simple potentials such as the SW and TF potentials, δ_0 depends only on the depth and range of the scattering potential under study⁶³. From Eq. 7 it is then possible to fix the TF potential's parameters V_0^{TF}, q in terms of V_0, a relative to the SW potential, so that the former yields the same s-wave shifts δ_0 caused by the SW potential. Note that this approach is often called the shape independent approximation (SIA). To implement the SIA, one needs to compute c_0, r_0 for both potentials. By their comparison, one finds the following relations $V_0^{\text{TF}} = (1/3)(5/2)^{3/2} V_0, q = (5/2)^{1/2} a^{-1}$. Next, we can represent a given instance of a SW potential, labelled by δ_0 according to Eq. 2, by the image of a TF potential whose parameters satisfy the above SIA's relations.

In panels (a), (b) of Fig. 7 the scatter plots of the prediction versus the reference s-wave phase shift according to the SIA applied to the SW potential⁷⁵, at $k = 0.01, 0.1$, respectively, are shown. We found MAPE is 0.92%, 0.18%, for $k = 0.01, 0.1$ respectively. Therefore this scattering approximation combined with our ML model can be used to yield satisfactory accurate predictions of δ_0 even for nonrelativistic collisions in the presence of a square-well potential.

Our analysis suggests that our ML model is effectively learning the phase functions after being trained on the scattering potential images X_μ labelled by the respective phase shift $\delta_0^{(\mu)}$.

III. SUMMARY AND OUTLOOK

We presented a CNN model for learning the s-wave phase shifts arising from four different three-dimensional spherically symmetric potentials. The good machine learning performance achieved by our model demonstrates that the Hamiltonian can serve as a guiding principle in the construction of a physically-motivated descriptor.

Moreover, we tried to understand how the CNN's learning tasks vary with the functional complexity of the phase function emerging in the presence of different potentials. To this aim, we add a number of instances of the Thomas-Fermi potential supporting bound states to the respective data set. In such a case, we found that the CNN's regression task becomes difficult requiring a substantial increase of the number of epochs for reaching a good performance. We argue that this larger number of epochs mainly arises from the steepness of the mapping $r \mapsto \delta_0(r)$ as a direct consequence of the Levinson's theorem, thereby hindering the CNN's learning task.

The next goal could be to build a supervised machine learning model able to predict δ_l with $l = 1, 2, \dots$ at fixed collision energy by including the centrifugal potential contribution into the descriptor in a similar way that we discussed here. However, a more ambitious goal would be to effectively learning $r \mapsto \delta_l(r, k)$ having the wave number k as additional input in the model.

ACKNOWLEDGMENTS

We thank professor Ravi Rau for pointing out important works regarding the phase amplitude equation and dr. Jan Hermann for valuable comments and suggestions. This work was supported by the EU through the European Regional Development Fund CoE program TK133 “The Dark Side of the Universe”.

AUTHOR CONTRIBUTION STATEMENT

Both authors contributed equally to this study.

DATA AVAILABILITY

The data that support the findings of this study are available from the corresponding author upon reasonable request.

* alessandro.romualdi@yahoo.com

† gionnimarchetti@ub.edu

¹ C. J. Joachain, *Quantum Collision Theory* (North-Holland, 1975).

² H. Piel and M. Chrysos, *Molecular Physics* **118**, e1587024 (2020).

³ E. Fermi, *Ric. Scientifica* **7** (1936).

⁴ K. Huang and C. N. Yang, *Phys. Rev.* **105**, 767 (1957).

⁵ Z. Idziaszek and T. Calarco, Phys. Rev. Lett. **96**, 013201 (2006).

⁶ J.-C. Pain, Journal of Physics Communications **2**, 025015 (2018).

⁷ W. Kohn, Phys. Rev. **74**, 1763 (1948).

⁸ R. K. Nesbet, Phys. Rev. **175**, 134 (1968).

⁹ F. Calogero, Il Nuovo Cimento (1955-1965) **27**, 261 (1963).

¹⁰ F. Calogero, *Variable Phase Approach to Potential Scattering* (Academic Press, 1967).

¹¹ V. V. Babikov, Soviet Physics Uspekhi **10**, 271 (1967).

¹² U. Fano and A. R. P. Rau, *Atomic Collisions and Spectra* (Academic Press, Inc., Orlando, Florida, 1986).

¹³ A. Palov and G. Balint-Kurti, Computer Physics Communications **263**, 107895 (2021).

¹⁴ L. Zdeborová, Nature Physics **13**, 420 (2016).

¹⁵ G. Carleo, I. Cirac, K. Cranmer, L. Daudet, M. Schuld, N. Tishby, L. Vogt-Maranto, and L. Zdeborová, Rev. Mod. Phys. **91**, 045002 (2019).

¹⁶ J. Schmidt, M. R. G. Marques, and M. A. L. Botti, Silvana. Marques, npj Computational Materials **5**, 489 (2016).

¹⁷ F. A. Faber, L. Hutchison, B. Huang, J. Gilmer, S. S. Schoenholz, G. E. Dahl, O. Vinyals, S. Kearnes, P. F. Riley, and O. A. von Lilienfeld, Journal of Chemical Theory and Computation **13**, 5255–5264 (2017).

¹⁸ A. P. Bartók, S. De, C. Poelking, N. Bernstein, J. R. Kermode, G. Csányi, and M. Ceriotti, Sci Adv. **3**, e1701816 (2017).

¹⁹ G. Montavon, M. Rupp, V. Gobre, A. Vazquez-Mayagoitia, K. Hansen, A. Tkatchenko, K.-R. Müller, and O. A. von Lilienfeld, New Journal of Physics **15**, 095003 (2013).

²⁰ M. Rupp, A. Tkatchenko, K.-R. Müller, and O. A. von Lilienfeld, Phys. Rev. Lett. **108**, 058301 (2012).

²¹ K. T. Schütt, H. Glawe, F. Brockherde, A. Sanna, K. R. Müller, and E. K. U. Gross, Phys. Rev. B **89**, 205118 (2014).

²² L. Wang, Phys. Rev. B **94**, 195105 (2016).

²³ J. Carrasquilla, R. Melko, Nature Phys **13**, 431–434 (2017).

²⁴ E. van Nieuwenburg, E. Bairey, and G. Refael, Phys. Rev. B **98**, 060301 (2018).

²⁵ J. Behler and M. Parrinello, Phys. Rev. Lett. **98**, 146401 (2007).

²⁶ A. P. Bartók, M. C. Payne, R. Kondor, and G. Csányi, Phys. Rev. Lett. **104**, 136403 (2010).

²⁷ A. P. Thompson, L. P. Swiler, C. R. Trott, S. M. Foiles, and G. J. Tucker, Journal of Computational Physics **285**, 316 (2015).

²⁸ A. V. Shapeev, Multiscale Modeling & Simulation **14**, 1153 (2016).

²⁹ J. Behler, The Journal of Chemical Physics **145**, 170901 (2016), <https://doi.org/10.1063/1.4966192>.

³⁰ J. Hermann, Z. Schätzle, and F. Noé, Nature Chemistry **12**, 891 (2020).

³¹ S. Manzhos, Machine Learning: Science and Technology **1**, 013002 (2020).

³² L. M. Ghiringhelli, J. Vybiral, S. V. Levchenko, C. Draxl, and M. Scheffler, Phys. Rev. Lett. **114**, 105503 (2015).

³³ A. P. Bartók, R. Kondor, and G. Csányi, Phys. Rev. B **87**, 184115 (2013).

³⁴ K. Rossi and J. Cumby, International Journal of Quantum Chemistry **120**, e26151 (2020).

³⁵ F. Musil, A. Grisafi, A. P. Bartók, C. Ortner, G. Csányi, and M. Ceriotti, Chemical Reviews **121**, 9759 (2021).

³⁶ D. J. Gross, Proc. Natl. Acad. Sci USA **93**, 14256 (1996).

³⁷ P. Hohenberg and W. Kohn, Phys. Rev. **136**, B864 (1964).

³⁸ O. A. von Lilienfeld, International Journal of Quantum Chemistry **113**, 1676 (2013).

³⁹ K. Mills, M. Spanner, and I. Tamblyn, Phys. Rev. A **97** (2018).

⁴⁰ D. Yarotsky, CoRR [abs/1804.10306](https://arxiv.org/abs/1804.10306) (2018), arXiv:1804.10306.

⁴¹ D. Hubel and T. N. Wiesel, J Physiol. **160**, 106 (1962).

⁴² K. Fukushima, Biological Cybernetics **36**, 193–202 (1980).

⁴³ Y. Lecun, L. Bottou, Y. Bengio, and P. Haffner, Proceedings of the IEEE **86**, 2278 (1998).

⁴⁴ A. Krizhevsky, I. Sutskever, and G. E. Hinton, in *Advances in Neural Information Processing Systems*, Vol. 25, edited by F. Pereira, C. J. C. Burges, L. Bottou, and K. Q. Weinberger (Curran Associates, Inc., 2012) pp. 1097–1105.

⁴⁵ C. Szegedy, Wei Liu, Yangqing Jia, P. Sermanet, S. Reed, D. Anguelov, D. Erhan, V. Vanhoucke, and A. Rabinovich, in *2015 IEEE Conference on Computer Vision and Pattern Recognition (CVPR)* (2015) pp. 1–9.

⁴⁶ D. Silver, A. Huang, C. J. Maddison, A. Guez, L. Sifre, G. van den Driessche, J. Schrittwieser, I. Antonoglou, V. Panneershelvam, M. Lanctot, S. Dieleman, D. Grewe, J. Nham, N. Kalchbrenner, I. Sutskever, T. Lillicrap, M. Leach, K. Kavukcuoglu, T. Graepel, and D. Hassabis, Nature **529**, 489 (2016).

⁴⁷ S. Mallat, Philosophical Transactions of the Royal Society A: Mathematical, Physical and Engineering Sciences **374**, 20150203 (2016).

⁴⁸ H. W. Lin, M. Tegmark, and D. Maddison, Rolnick, Journal of Statistical Physics **168**, 1223 (2017).

⁴⁹ N. W. Ashcroft and M. D. Mermin, *Solid State Physics* (Saunders College, Philadelphia, 1976).

⁵⁰ J. R. Meyer and F. J. Bartoli, Phys. Rev. B **23**, 5413 (1981).

⁵¹ G. Giuliani and G. Vignale, *Quantum Theory of Electron Liquid* (Cambridge University Press, Cambridge, UK, 2005).

⁵² B. Pohv, K. Rith, C. Scholz, and F. Zetsche, *Particles and Nuclei*, 1st ed. (Springer, Berlin, 2002).

⁵³ N. F. Bali, S.-Y. Chu, R. W. Haymaker, and C.-I. Tan, Phys. Rev. **161**, 1450 (1967).

⁵⁴ I. Nagy and B. Apagyi, Phys. Rev. A **58**, R1653 (1998).

⁵⁵ C. S. Lam and Y. P. Varshni, Phys. Rev. A **6**, 1391 (1972).

⁵⁶ P. K. Shukla and B. Eliasson, Physics Letters A **372**, 2897 (2008).

⁵⁷ P. K. Shukla and B. Eliasson, Phys. Rev. Lett. **108**, 165007 (2012).

⁵⁸ Lin, C. Y. and Ho, Y. K., Eur. Phys. J. D **57**, 21 (2010).

⁵⁹ Z. Moldabekov, T. Schoof, P. Ludwig, M. Bonitz, and T. Ramazanov, Physics of Plasmas **22**, 102104 (2015).

⁶⁰ Y. Y. Qi, J. G. Wang, and R. K. Janev, Physics of Plasmas **23**, 073302 (2016).

⁶¹ D. Munjal, P. Silotia, and V. Prasad, Physics of Plasmas **24**, 122118 (2017).

⁶² K. S. Krane, *Introductory Nuclear Physics* (John Wiley and Sons, U.S.A, 1988).

⁶³ A. Z. Capri, *Nonrelativistic Quantum Mechanics*, 3rd ed. (World Scientific, Singapore, 2002).

⁶⁴ J. R. Taylor, *Scattering Theory: The Quantum Theory of Nonrelativistic Collisions* (John Wiley & Sons, Inc., New York, 1972).

⁶⁵ P. H. E. Meijer and J. L. Repace, American Journal of Physics **43**, 428 (1975).

⁶⁶ P. M. Morse and W. P. Allis, Phys. Rev. **44**, 269 (1933).

⁶⁷ G. Marchetti, *Journal of Applied Physics* **126**, 045713 (2019).

⁶⁸ K. Chadan, R. Kobayashi, and T. Kobayashi, *Journal of Mathematical Physics* **42**, 4031 (2001).

⁶⁹ N. Levinson, *Kgl. Danske Videnskab.Selskab., Mat.fys. Medd.* **25** (1949).

⁷⁰ M. Portnoi and I. Galbraith, *Solid State Communications* **103**, 325 (1997).

⁷¹ H. A. Bethe, *Phys. Rev.* **76**, 38 (1949).

⁷² L. Petzold, *SIAM Journal on Scientific and Statistical Computing* **4**, 136 (1983).

⁷³ M. Abadi, P. Barham, J. Chen, Z. Chen, A. Davis, J. Dean, M. Devin, S. Ghemawat, G. Irving, M. Isard, M. Kudlur, J. Levenberg, R. Monga, S. Moore, D. G. Murray, B. Steiner, P. Tucker, V. Vasudevan, P. Warden, M. Wicke, Y. Yu, and X. Zheng, in *Proceedings of the 12th USENIX Conference on Operating Systems Design and Implementation*, OSDI'16 (USENIX Association, USA, 2016) p. 265–283.

⁷⁴ D. P. Kingma and J. Ba, “Adam: A method for stochastic optimization,” (2014).

⁷⁵ Note that in this case, using the same model hyperparameters as in the previous cases, resulted in higher variability in validation loss during training. We regularized the model by reducing the learning rate of the Adam optimizer to 10^{-6} and increasing the training epochs increased to 5000.